Machine learning study of magnetism in uranium-based compounds

Ayana Ghosh [1,2,*] Filip Ronning [3] Serge M. Nakhmanson [1] and Jian-Xin Zhu [2,4,†]

[1]*Department of Materials Science & Engineering and Institute of Materials Science, University of Connecticut, Storrs, Connecticut 06269, USA*

[2]*Theoretical Division, Los Alamos National Laboratory, Los Alamos, New Mexico 87545, USA*

[3]*Institute for Materials Science, Los Alamos National Laboratory, Los Alamos, New Mexico 87545, USA*

[4]*Center for Integrated Nanotechnologies, Los Alamos National Laboratory, Los Alamos, New Mexico 87545, USA*

(Received 12 May 2020; accepted 4 June 2020; published 19 June 2020)

Actinide and lanthanide-based materials display exotic properties that originate from the presence of itinerant or localized f electrons and include unconventional superconductivity and magnetism, hidden order, and heavy-fermion behavior. Due to the strongly correlated nature of the $5f$ electrons, magnetic properties of these compounds depend sensitively on applied magnetic field and pressure, as well as on chemical doping. However, precise connection between the structure and magnetism in actinide-based materials is currently unclear. In this investigation, we established such structure-property links by assembling and mining two datasets that aggregate, respectively, the results of high-throughput density functional theory simulations and experimental measurements for the families of uranium- and neptunium-based binary compounds. Various regression algorithms were utilized to identify correlations among accessible attributes (features or descriptors) of the material systems and predict their cation magnetic moments and general forms of magnetic ordering. Descriptors representing compound structural parameters and cation f-subshell occupation numbers were identified as most important for accurate predictions. The best machine learning model developed employs the random forest regression algorithm. It can predict both spin and orbit moment size with root-mean-square error of $0.17\mu_B$ and $0.19\mu_B$, respectively. The random forest classification algorithm is used to predict the ordering (paramagnetic, ferromagnetic, and antiferromagnetic) of such systems with 76% accuracy.

DOI: 10.1103/PhysRevMaterials.4.064414

I. INTRODUCTION

Big-data-driven approaches employing supervised, semisupervised, or unsupervised machine learning algorithms are becoming tools of choice in materials physics, chemistry, and engineering for the task of establishing yet unknown structure-property-performance relationships that may exist within a given family or class of materials [1–5]. The success of these tools in elucidating hidden connections between the material or molecular structure and the resulting behavior can be attributed to growing availability of databases collating theoretical and experimental materials data across disciplines. In particular, databases aggregating the results of density functional theory (DFT) computations, which provide a reasonable compromise between high accuracy and computational costs and can also process fictitious materials structures, are especially popular as components of prediction-driven strategies for materials design and discovery [6,7]. A nonexhaustive list of examples demonstrating applications of machine learning algorithms in materials science includes multiple investigations conducted for the families of technologically critical (energy harvesting, storage, and efficiency [8–16], catalysis [17], photovoltaics [18], etc.) and pharmaceutical (drug design [19,20], reaction mechanisms [21–24], etc.) compounds.

In addition to more generic traits originating from their general chemistry and radioactive behavior, lanthanide and actinide-based materials exhibit a range of exciting properties associated with the filling of the $4f$ and $5f$ electron subshells. In particular, the interplay of the hybridization of $4f$ and $5f$ electrons with itinerant conduction electrons and the onsite Coulomb repulsions among those electrons are responsible for the behavior exhibited by lanthanides and actinides. Their properties of interest include an emergence of magnetism [25–29], unconventional superconductivity [30–36], metal-insulator transitions [37–43], hidden magnetic order [44–49], and the presence of heavy fermions [50–60]. Due to strong correlation effects involving $5f$ electrons and their interactions with itinerant conduction electrons, magnetic behavior of actinide-based systems is sensitive to applied pressure, magnetic field, and chemical doping. As a result, actinide-based materials are not only useful in nuclear applications, but also constitute a convenient playground to develop our fundamental understanding of correlated materials. So far, only the $4f$-electron magnetism has been studied with DFT-based machine learning (ML) tools in a general context of ternary oxide compounds [61,62]. A focused study of magnetic properties in $5f$-electron materials has not yet been reported.

The main purpose of this work is a systematic investigation of possible connections between the structure and magnetic properties for a variety of different actinide-based compounds in an attempt to establish a general prescription for constructing families of ML models that incorporate computational and experimental knowledge. Complementary utilization of data

*ayana.ghosh@uconn.edu

†jxzhu@lanl.gov

originating from both of these sources is necessary for accurate assessment and prediction of the magnetic properties of interest: average cation moment sizes (but not their ordering, which is intricately complex for theoretical simulations) can be easily extracted from DFT calculations, while magnetic ordering can be straightforwardly characterized by experiments. The 12 compounds chosen for compiling dataset I (computational) exhibit either A-type or C-type antiferromagnetism (AFM) or ferromagnetism (FM). As further explained in Sec. II A and validated in Sec. III, we use only AFM configurations for building this . Dataset II (experimental) is assembled by extracting information on magnetic ordering in uranium-based binary compounds from numerous literature sources. The acquired information serves not only as a base for constructing ML models capable of predicting magnetic ordering, but in some instances can also provide the necessary validation for the models utilizing only computational data. We also note that there are caveats in the experimental data, which naturally translate into limitations on the predictive accuracy of ML models. In most cases, only the major forms of magnetic ordering, i.e., paramagnetism (PM), FM, or AFM (denoted as *classes* in classification models), are reported, while information about the specific types of AFM or PM, or the orientation of magnetic moments with respect to crystallographic axes, is not given. The flowchart shown in Fig. 1 outlines the main stages involved in the development of the ML models utilized in this study. These stages include compilation and curation of appropriate datasets, performing data analysis with standard data mining tools, construction of the models and their following internal and external validation.

In order to predict the magnetic moment sizes, we have developed our ML-based framework focusing on *regression*-type algorithms. Five different algorithms [63], including linear regression (LR), least absolute shrinkage and selection operator (LASSO), kernel ridge regression (KRR), random forest regression (RFR), and support vector machine regression (SVMR) were chosen systematically to evaluate the performance of the models. We have also utilized random forest classification (RFC) algorithm to predict the probabilities of each compound exhibiting PM, FM, or AFM ordering. We note that the choice of these algorithms [64] is driven by transferability, simplicity of implementation, as well as compliance with the best practices in this area of research.

The main findings of our study are summarized as follows: (a) ML frameworks employing regression and classification algorithms can be utilized to predict magnetic moment size and ordering in uranium-based binary compounds. (b) Various descriptor sets, depending on the availability of data sources (both computational and experimental), can be designed to construct families of meaningful ML models. (c) While ML models can identify the most important descriptors pertinent to the end points, complementary data analysis can establish quantitative structure-property relationships (e.g., cutoff values of lattice parameters for a compound to exhibit PM, FM, or AFM ordering) present in such materials. (d) It is often possible to identify physical phenomena underpinning the results obtained from ML models (e.g., exchange interactions that lead to particular types of magnetic behavior).

The rest of the paper is organized as follows: Section II reviews the standard methodology utilized for dataset acquisition and curation, as well as for the ML model building. Section III presents the results of the statistical analysis of the contents of both datasets, followed by a discussion of predictive capabilities of the developed ML models for evaluating cation magnetic moment size and magnetic ordering in uranium- and neptunium-based compounds. In addition, we compare the utility of regression- and classification-based frameworks for predicting both moment size and ordering. Finally, some concluding remarks are provided in Sec. IV.

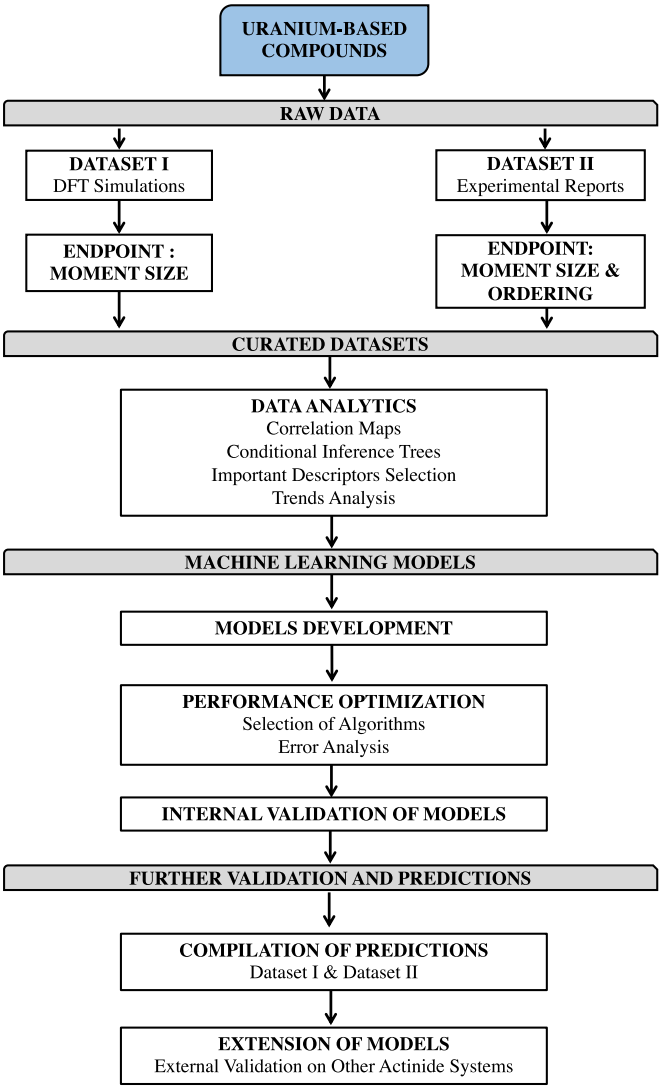

FIG. 1. Flowchart outlining the main development stages involved in construction and validation of ML models for predicting cation magnetic moment size and magnetic ordering in actinide-based binary systems. Primary stages are shown as gray rectangles, while any necessary secondary stages are represented by white rectangles. Some of the diagram elements introduced here are analyzed in further detail in Fig. 2(b) and accompanying text.

II. METHODS

A. Datasets

First-principles calculations of average spin and orbital moments were performed using the projector augmented

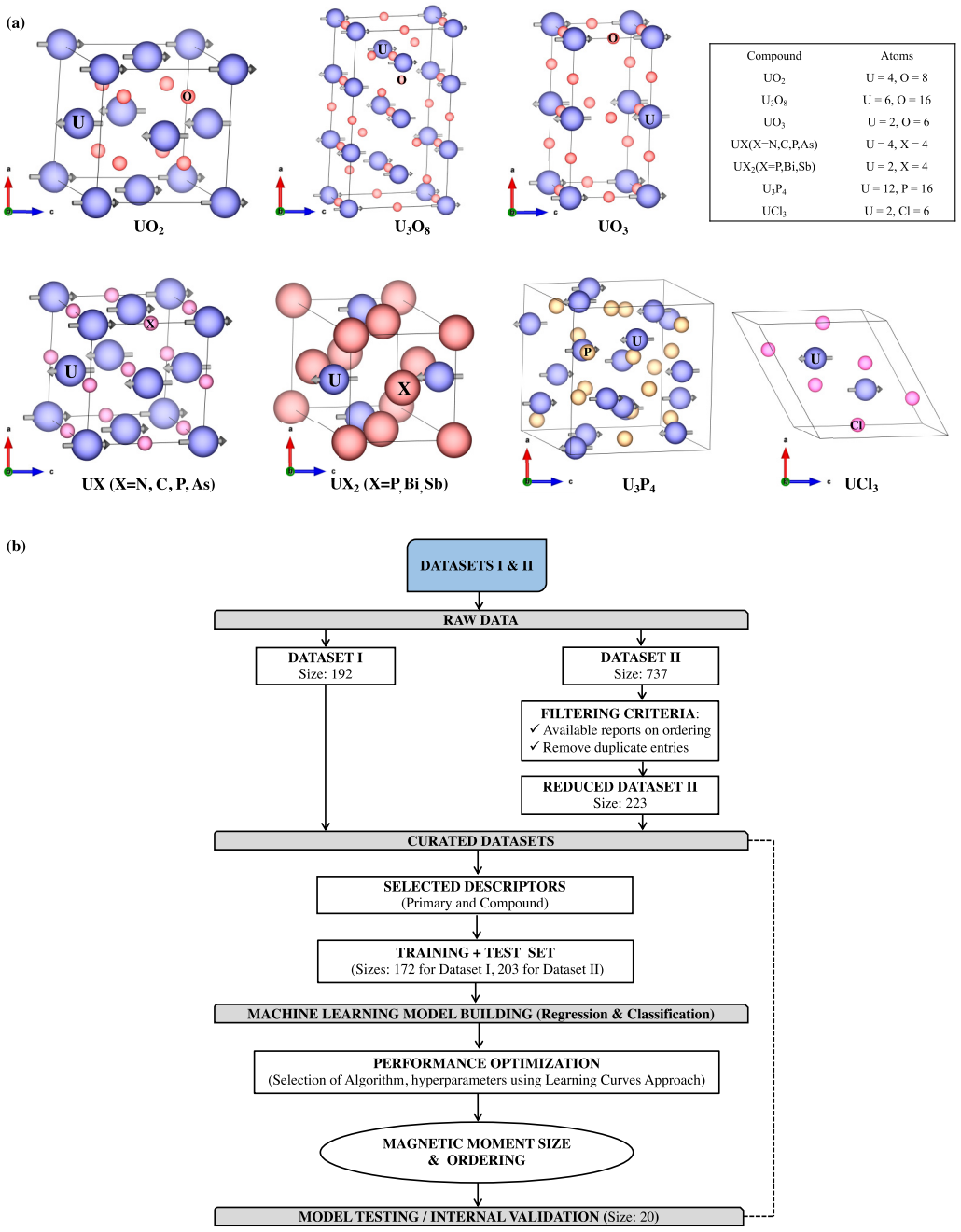

FIG. 2. Structural models of 12 uranium-based binary compounds that were assumed in DFT computations for creating dataset I. The AFM I configurations are shown using a vector representation, where directions of magnetic moments on U cations are alternating between consecutive uranium layers and their orientation is along the crystal c axis. (b) Flowchart showing the stages of development of ML models to predict both moment size and ordering.

plane-wave (PAW) method implemented in the Vienna *ab initio* simulation package (VASP) [65,66]. The generalized gradient approximation (GGA) was adopted to represent the exchange and correlation interactions, with the GGA+U_{eff} [67] approach utilized to capture the strongly correlated nature of the 5f electrons. All computations were carried out with a 500-eV plane-wave cutoff energy using tetrahedron method with Blochl corrections with appropriate Monkhorst-Pack [68] k-point meshes, which produced well-converged results.

For the construction of dataset I, which is built only on the data extracted from the DFT simulations, the following 12 uranium-based binary compounds were utilized: UO_2, U_3O_8, UO_3, UN, UC, UP, UP_2, U_3P_4, UAs, UBi_2, USb_2, and UCl_3. The magnetic structures of these compounds are well documented in the literature [69–72], which is the primary motivation behind choosing them to build dataset I. Geometrical structures with AFM I configuration for all of these compounds are shown in Fig. 2(a). For each compound, initial lattice parameters and ionic positions were obtained

from inorganic crystal structure database (ICSD) [73], after which eight individual variants were created by varying the Hubbard parameter U_{eff} between 0 and 6 eV in 2-eV increments in the presence or absence of spin-orbit coupling. U_{eff} values from the same range have been used previously in a number of DFT-based investigations of actinide compounds. Electronic and magnetic properties for each of the eight variants were evaluated both for the ICSD-provided structural parameters and after optimization, which included relaxing the unit-cell shape and volume to stresses below 0.1 kbar and all the ionic positions until the associated Hellman-Feynman forces were below 10^{-3} eV/Å. Utilization of data generated using structural parameters obtained from both ICSD and DFT computations allowed us to incorporate information of varying fidelity [74] levels into our ML models, which is in turn helpful for consistent evaluation and improvement of their predictive accuracy. We note that structural configurations obtained from DFT computations belong to the same space groups as those reported in ICSD. Although it is possible to create multiple other structures by directly varying lattice parameters and internal positions of atoms, the descriptor space of dataset I will not be significantly altered. Therefore, inclusion of such additional entries into dataset I will not help improve predictive capabilities of the resulting ML models.

For all computations involved in generating dataset I, we considered a specific type of AFM ordering, namely AFM I, where the directions of magnetic moments on U cations are alternating between consecutive uranium layers and their orientation is along the crystalline c axis, as shown in Fig. 2(a). We restricted ourselves to studying just one magnetic configuration type since our primary interest is in estimating moment sizes only, and these do not change significantly if other configurations (e.g., out-of-plane spin orientation) are selected instead. The chosen initial AFM configurations for all compounds except U_3P_4 are in accordance with those reported in the literature [69–72]. For U_3P_4, a FM configuration has lower energy, as compared to that in AFM I. This is confirmed by DFT+U_{eff} (=4eV) computations showing the energy difference of ∼3.26 eV between these two magnetic configurations. The energy tradeoffs between choosing a-axis versus c-axis orientation of the magnetization for all 12 compounds are listed in Table I.

We report nominal differences ($<0.3\mu_B$) of the magnetic moment between these two magnetization directions of the same AFM I configuration as compared to average spin ($1.64\mu_B$) and orbital ($2.82\mu_B$) moment sizes for all of the chosen compounds. The energy is related to the magnetic moment size. Hence, the resulting energy differences are not significant either. We note that for the cubic systems, the magnetization along a axis or c axis should be equivalent. This implies that the energy differences as reported in Table I are due to numerical uncertainty. Overall, dataset I was built solely using DFT simulations and comprises 16 variants for every compound, for a total of 192 entries.

Dataset II was constructed by curating the results of 737 experimental reports of standard quality on uranium-based binary compounds, as found in the ICSD [73]. Only structures stable at low temperature were considered, while data on any metastable high-temperature configurations were discarded.

TABLE I. Differences in energy and average moment sizes between a-axis and c-axis moment orientations for all 12 compounds present in dataset I. Spin-orbit coupling and $U_{\text{eff}} = 4$ eV were used in these computations.

Compound	ΔE (eV)	$\Delta\mu_{\text{spin}}(\mu_B)$	$\Delta\mu_{\text{orbit}}$ (μ_B)
UO_2	0.032	0.001	−0.009
U_3O_8	0.044	0.071	−0.011
UO_3	0.096	0	0
UN	0.007	0.015	−0.037
UC	0.069	0.054	−0.074
UP	−0.003	−0.090	−0.068
UAs	−0.002	−0.006	−0.02
UP_2	−0.206	0.008	−0.036
UBi_2	0.032	0.029	0.023
USb_2	0.024	0.028	0.038
U_3P_4	0.067	−0.011	0.087
UCl_3	0.279	−0.009	−0.011

After the removal of duplicate entries, 223 data points including information on magnetic properties (cation moment size and ordering) remained in the dataset. These compounds were also categorized into three classes according to the nature of the reported magnetic ordering: (1) PM, i.e., compounds with local magnetic moment but no long-range order present, (2) FM, i.e., compounds with magnetic spins aligned in the same directions, and (3) AFM A type or C type.

The sizes of both datasets before and after curation, as well as the filtering criteria for dataset II are shown in the top part of the ML model development flowchart in Fig. 2(b). For each dataset, 20 entries were kept aside for internal validations and the rest (172 for dataset I and 203 for dataset II) were used for training (90%) and testing (10%) of ML models.

B. Descriptors

For dataset I, the following eight primary descriptors were considered: lattice parameters ($\frac{\text{magnetic unit cell parameters}}{\sqrt[3]{\text{number of actinide elements}}}$) *alatt*, *blatt,* and *clatt* (Å), atomic volume ($\frac{\text{magnetic unit cell lattice parameters}}{\text{number of actinide elements}}$) *volume* (Å^3), Hubbard parameter U_{eff} (eV), spin-orbit-coupling strength SOC (eV), cation $5f$-subshell occupation number (number of total valence electrons of actinide element, valence of anion) $N_{\text{occ}}(5f)$, and system Fermi energy level En_F (eV). For each primary descriptor x, additional compound descriptors were generated using 10 prototypical functions, namely, x^2, x^3, $\exp(x)$, $\sin(x)$, $\cos(x)$, $\tan(x)$, $\sinh(x)$, $\cosh(x)$, $\tanh(x)$, and $\ln(x)$, to allow for possible nonlinearities in the connections between the descriptor and end-point properties.

The descriptor space for dataset II contains all structural parameters (as defined above), number of formula units, and $N_{\text{occ}}(5f)$, all extracted from the respective experimental reports. Furthermore, for every entry in dataset II, a matrix representation called orbital field matrix (OFM) [75,76], as implemented in a Python library [77], was computed using distances between coordinating atoms, valence shells, and Voronoi polyhedra weights, which provided information on the chemical environment of each atom in the unit cell. The

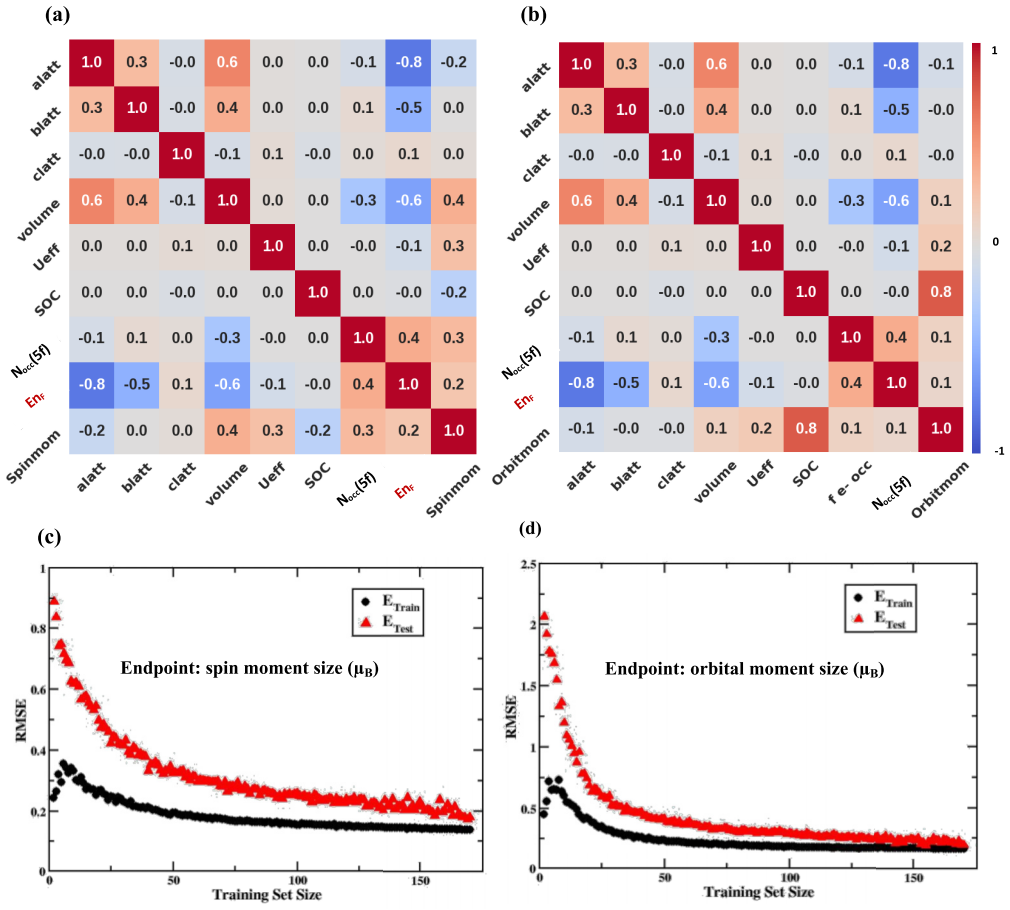

FIG. 3. Correlation matrices representing Pearson correlation coefficients for primary descriptors applicable to dataset I for (a) spin moment size and (b) orbital moment size end points. The primary descriptor space for dataset I consists of eight features: lattice parameters *alatt*, *blatt,* and *clatt*, and *volume*, Hubbard parameter U_{eff}, spin-orbit coupling strength SOC, cation $5f$-subshell occupation number $N_{\text{occ}}(5f)$, and system Fermi energy level En_F. *We note that the* En_F *descriptor was not used in the ML model construction, as described later in Sec. III.* Learning curves for two ML models predicting (c) spin moment size and (d) orbital moment size constructed using the RFR algorithm. E_{Train} and E_{Test} refer to average training and test set root-mean-square errors. The average % mean absolute test errors in predicting spin (c) and orbital (d) moment sizes are 14% and 17%.

OFM elements are defined as following [75,76]:

$$X_{ij}^{\prime p} = \sum_{k=1}^{n_p} o_i^p o_j^k \frac{\theta_k^p}{\theta_{\max}^p} \zeta(r_{pk}), \tag{1}$$

where $i, j \in D = (s^1, s^2, \ldots, f^{14})$ for central i and coordinating j orbitals, respectively; o_i^p and o_j^k are elements of one-hot basis vectors (i or j) of the electronic configuration with central atom indexed by p and neighboring atom indexed by k. Here, the one-hot basis vectors are understood in the sense that we only consider the valence orbitals. The weight of the atom k in the coordination of the central atom at site p is given by $\theta_k^p/\theta_{\max}^p$, where θ_k^p is the solid angle determined from the respective Voronoi polyhedron. The number of nearest-neighbor atoms surrounding atom site p is n_p. The size and distance-dependent weight function is also included as $\zeta(r_{pk})$.

C. Data analytics

Prior to the development of ML models, both datasets were analyzed using standard data analytics techniques to determine the presence of any relationships between the structural descriptors and the targeted magnetic properties. Any inferences drawn from this analysis may provide useful insight for choosing appropriate descriptor space and algorithms for the ML model development. The primary descriptor sets for dataset I were subjected to a Pearson correlation filter to remove features that exhibit a high correlation with the other descriptors within the same set, as shown in Fig. 3. The same approach was also applied to the combined set of primary and compound descriptors. Additionally, for dataset I we employed a conditional inference procedure with Bonferroni-corrected significance (p value < 0.05) value, used as the splitting criteria (stopping rules) for each node while constructing trees as implemented in R version 3.4.2 via CTree algorithm [78]. The splitting process was continued recursively throughout the whole dataset I. The results of this analysis along with correlation matrices for secondary features are presented in the Supplemental Material [79].

We utilized all 223 entries in dataset II to perform median analysis. The dataset was divided into two subsets (below and above the median value) based on the median value for each descriptor. For every descriptor, magnetic ordering class

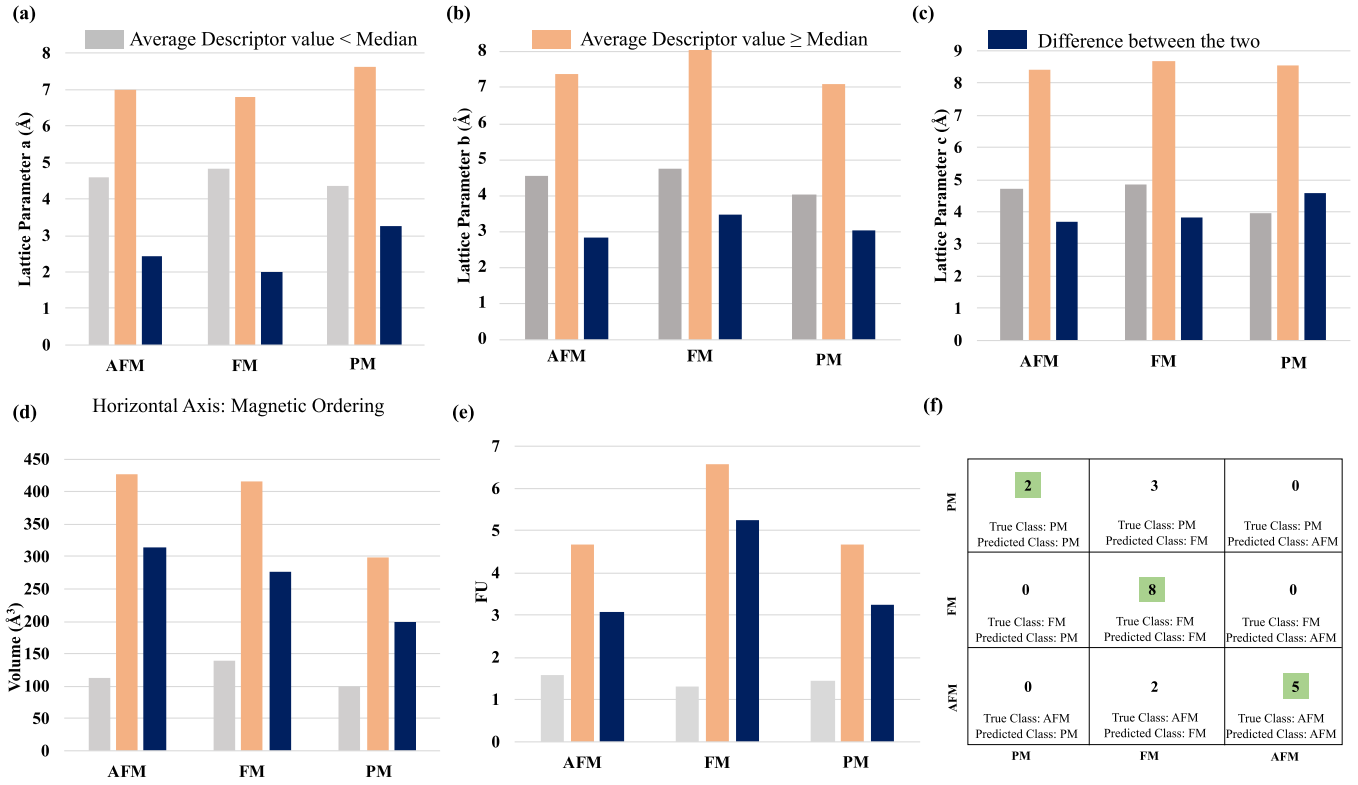

FIG. 4. Dataset II was divided into two sets: below median value (gray), above median value (orange). The difference between these two sets for all experimental descriptors is represented by the blue bar. The considered features were (a)–(c) lattice parameters (Å) in all directions, (d) cell volume (Å^3), (e) formula units (FU). The grouping was done based on the respective medians and type of magnetic ordering reported. The median values for these features are (a) 5.588 Å, (b) 5.5 Å, (c) 5.62 Å, (d) 191.85 Å^3, and (e) 4. The ML-based prediction with 76% average accuracy on the test set (20 entries) for dataset II is given by the confusion matrix in (f). Here, the highlighted boxes denote the number of compounds for which the magnetic ordering class was predicted correctly.

was assigned to the respective entries belonging to the two resultant subsets. Bar charts shown in Figs. 4(a)–4(e) report the differences between the mean values of the descriptors. Larger differences observed for any particular descriptor are likely to produce an increased variance in the end point when that descriptor is used for construction of ML models.

D. Algorithms

Five regression algorithms, including LR, LASSO, KRR, RFR, SVMR as implemented in Scikit-learn Python [80] version 3.5.2, were employed to construct ML models from dataset I. Regression-based algorithms were chosen over classification-based ones, as the end point of interest (magnetic moment size) was computed numerically for each entry in respective datasets. The RFC classification algorithm was also utilized to construct ML models for predicting the magnetic ordering end point. Optimized hyperparameters used for all six algorithms are presented in the Supplemental Material [79].

E. ML model development and validation

One of the main concerns of conventional ML model development is selection of the dataset size. Here, for both datasets, the number of entries was restricted to less than 230 entries, which may potentially limit the accuracy of the resulting models. The standard deviations in the predicted values for the test sets may be as large as 5%–10%, making any comparisons originating from a single set of predictions misleading (see Supplemental Material [79], where two such cases are compared). In order to avoid any statistical bias, we built learning curves, such as ones shown in Fig. 3, by varying the training set size in order to estimate the performance of all the developed models. For each point on the learning curve [19], the average RMSE is calculated using 1000 randomly generated (by sampling with replacement) training and test set evaluations. The average RMSE for a training set size N is denoted $E_{\text{Train}}(N)$, whereas for the corresponding test set it is denoted $E_{\text{Test}}(N)$, however, in this case the size of the set is now the total number of points minus N. The test set RMSE provides the expected error for a given model, while the difference between $E_{\text{Test}}(N)$ and $E_{\text{Train}}(N)$ is an estimation of how much variance or overfitting the model contains.

We have used confusion (error) matrices [80] to evaluate the performance of the RF classification models. For the three classes, such as AFM, FM, and PM, these matrices show the predicted class of each compound together with its true class. Diagonal elements of a confusion matrix represent the number of compounds for which the predicted classes match the true classes.

Both models predicting the moment size and ordering were tested using the *internal* validation sets, i.e., 20 entries that

were kept aside on the model development stage [Fig. 2(b)]. Moreover, we also applied these models to three *external* sets of actinide-based binary and ternary compounds, for which information on either moment size or ordering is not widely available in literature. Validations on datasets composed of materials that are dissimilar to those used in model development provided more stringent testing of robustness and transferability of our ML models.

We note that the SOC descriptor (representing the strength of such coupling determined by the DFT computations for dataset I) was unavailable for the compounds present in the validation set. As an alternative way to include this interaction in our models, we considered SOC as being present (1) or absent (0) instead of including its strength value. The U_{eff} could also be varied manually in the descriptor space depending on its estimated value (eV) to capture the strong correlation effect among the f-orbital electrons. In addition, valence electron numbers for other atoms and OFM, as applicable to one of the *external* validation sets consisting of uranium-based ternary compounds, were also included in the feature space for testing models built on datasets I and II.

III. RESULTS AND DISCUSSION

Here, we discuss the results obtained from the preliminary data analysis and ML models applied to internal and external validation sets of datasets I and II. The discussion proceeds in a sequential order, with each primary step highlighted throughout the section. Additional technical details are provided in the Supplemental Material [79].

From the results of the *correlation analysis* presented in Fig. 3(a) for the set of primary features, it is evident that *volume*, $N_{\text{occ}}(5f)$, and E_F descriptors have large Pearson coefficients with respect to the spin moment size end point, suggesting that these features should be included in the descriptor space for building ML models to predict spin moment size. However, since the $N_{\text{occ}}(5f)$ and E_F descriptors are highly correlated to each other, we kept only the former as a primary descriptor. We note that the E_F descriptor obtained from the DFT computations is relative and can be placed anywhere in the energy band gap between the occupied and unoccupied states. Therefore, the $N_{\text{occ}}(5f)$ feature is more appropriate as a descriptor containing information related to the electron density of states, which is apparently important for predicting magnetic moment sizes. The SOC descriptor has the highest correlation coefficient with respect to the orbital moment size end point in the matrix, as shown in Fig. 3(b). This is expected for the primary feature that accounts for strong SOC originating from $5f$ shell electrons. This analysis, extended to space of primary and secondary features, allowed us to shortlist 61 features by excluding highly correlated ones (correlation factor >0.85). Next, the *conditional inference* procedure applied to dataset I shows that *alatt*, *volume*, U_{eff}, and SOC are the top features capable of grouping the data well for spin and orbital moment size as end points, respectively.

Median analysis. As explained in Sec. II C, we have used a different approach to analyze dataset II by determining medians and differences in average values of the features. Based on the median values of the five features, dataset II was divided into subgroups, which was followed by assignment of the corresponding magnetic ordering and calculation of the difference (variance) in average feature values for the subgroups, as shown in Figs. 4(a)–4(e). The median values for each of these experimental descriptors (*lattice parameters*, *volume*, *number of formula units*) are 5.588 Å, 5.5 Å, 5.62 Å, 191.85 Å^3, and 4, respectively. There are a total of 112 entries in the subgroup where *alatt* $\geqslant$ median value of *alatt*, out of which 24 are AFM, 44 are FM, and 44 are PM. For the similar subgroups formed by other features, such as *blatt*, *clatt*, *volume*, *number of formula units*, the number of entries are (26, AFM; 50, FM; 36, PM), (30, AFM; 46, FM; 36, PM), (24, AFM; 48, FM; 40, PM), and (42, AFM; 70, FM; 51, PM), respectively.

Both conditional inference-tree and median-variance methods suggest that the decision-tree type of algorithm may have better performance compared to other regression algorithms, if used to build ML models for predicting moment size. Overall, these investigations performed using standard data analytics techniques are useful for cultivating some advance knowledge about the available data and identification of features important to predicting end points, as well as any inconsistencies present in the datasets.

The results produced by the *ML models* for predicting the moment size are presented as learning curves in Figs. 3(c) and 3(d). For both cases, the RFR algorithm outperforms the other algorithms significantly, as shown in both Figs. 3(c) and 3(d) and Table II. The average spin moment size of compounds used for training these models is $1.64\mu_{\text{B}}$. For the orbital moment size, the average is $2.82\mu_{\text{B}}$, counting only the training data points computed by including the SOC. The total moment size can be obtained using the vector sum of both spin and orbital moments, pointed in the opposite direction to each other due to Hund's rule for f-electron shell that is less than half-filled. The average E_{Test} values in predicting spin and orbital moment size are $0.17\mu_{\text{B}}$ and $0.19\mu_{\text{B}}$, respectively, as mentioned in Table II. In both cases, the RFR algorithm overfits the data by approximately 4%. On the other hand, the LASSO, KRR, and SVMR algorithms display minimal overfitting but plateau at higher $E_{\text{Test}}(N)$, as shown by comparative learning curves. Furthermore, all of the ML models are performance optimized based on bias-variance tradeoffs, i.e., these models always yield the optimized moment size, when used for any other material including those not present in the training set.

The average accuracy in predicting magnetic ordering for the test set of dataset II is 76%, as displayed in Fig. 4(f) using a confusion matrix. The OFM representation plays a key role in significantly improving the model performance (accuracy improved by $\sim$15%) in predicting magnetic ordering by including information on the valence shells and local coordination environment of the system. For both the moment size and ordering end points, the most important features (structural parameters and f-subshell occupation numbers) identified by the ML models based on the RFR and RFC algorithms are the same as those found earlier by the data analytics techniques.

We have also compared the average nearest-neighbor distances (d_{U-U}) for every entry in dataset II to the Hill limit [81] that provides restrictions, under which magnetic ordering

TABLE II. Test set error $E_{\text{Test}}(N)$ and difference (overfitting) between the training $E_{\text{Train}}(N)$ and test set errors for the training set size $N = 50$ and the largest training test size N_{max}, as obtained from the learning curves constructed with five different regression algorithms. The predicted end points are magnitudes of spin and orbital magnetic moments in μ_B.

End point	Algorithm	$E_{\text{Test}}(50)$	$E_{\text{Test}} - E_{\text{Train}}(50)$	$E_{\text{Test}}(N_{\text{max}})$	$E_{\text{Test}} - E_{\text{Train}}(N_{\text{max}})$
Spin moment	LR	0.61	0.44	0.33	0.12
	LASSO	0.44	0.24	0.30	0.05
	KRR	0.30	0.08	0.28	0.03
	SVMR	0.84	0.04	0.83	0.01
	RFR	0.32	0.13	0.17	0.04
Orbital moment	LR	1.46	0.88	0.96	0.24
	LASSO	0.90	0.14	0.80	0.10
	KRR	1.07	0.4	0.96	0.21
	SVMR	1.01	0.06	0.94	0.05
	RFR	0.41	0.22	0.19	0.03

occurs in actinide systems (see Supplemental Material [79] for additional details). For $d_{U-U} < 3.4$ Å, intermetallic uranium compounds are PM at low temperatures. Such compounds still have local magnetic moments but no magnetic long-range order is present. Due to large overlap of 5f orbitals, compounds with $d_{U-U} > 3.6$ Å generally exhibit long-range FM or AFM ordering, localized at uranium ions. On the other hand, for smaller d_{U-U}, itinerant f-electron behavior is more dominant leading to temperature-independent PM ordering. Our results are in reasonable agreement with the above-mentioned Hill limit for uranium ions to exhibit specific type of ordering. This observation is important to establish a physical significance of lattice parameters, which are identified as features critical for predicting both the moment size and ordering. The average lattice parameters obtained from dataset I are comparable within 15% to entries present in dataset II that reportedly exhibit AFM ordering at low temperatures. This, along with results from median-variance analysis performed on dataset II, also provides quantitative measure for structural parameters to observe a specific type of magnetic ordering in high likelihood. For example, a uranium-based binary compound with *alatt* $\geqslant 5.58$ Å, is more likely to exhibit AFM ordering at low temperatures.

Three of the models were tested first on the *internal validation* sets kept aside within datasets I and II. We employed an approach comparable to the learning curves by reporting the average moment size and ordering for each entry, as obtained by averaging over 1000 ML model predictions. Figures 5(a) and 5(b) show predictions made on the *internal* validation set acquired using dataset I. The average RMSEs for the spin and orbital moment size predictions on the *internal* validation sets (for $U_{\text{eff}} = 4$ eV) are $0.20\mu_B$ and $0.25\mu_B$, respectively. For compounds, such as UN, USb_2, UO_2, UBi_2 and UP, total moment sizes are available in the literature, and can be used to compare the ML model predictions for $U_{\text{eff}} = 4$ and 6 eV, as shown in Fig. 5(c). The average RMSEs for the prediction of the total moment size for these compounds are $0.32\mu_B$ and $0.35\mu_B$ for $U_{\text{eff}} = 4$ and 6 eV, respectively. This analysis also highlights the dependence of moment size on U_{eff} that is captured by the ML models. The average prediction accuracy obtained using RFC for the internal validation set of dataset II is 70.2%. The numbers of entries belonging to the PM, FM, and AFM classes, for which the predictions have matched with the observed orderings, are 9, 2, and 2, respectively, as shown in Fig. 5(d).

Finally, to assess the performance and transferability of these models to other actinide systems, we have compiled three *external* validation sets, the first two containing uranium-based and neptunium-based binary and the third one containing uranium-based ternary compounds [82]. The results of these predictions using the same averaging technique as applied before to the *internal* validation sets are shown in Fig. 6. We note that although predictions of the *moment size* cannot be verified for these compounds due to the scarcity of experimental information, predictions of magnetic *ordering* that classify them as AFM, FM, or PM are comparable with those reported in the literature [82] without accounting for the exact spin textures.

External set I of binary compounds includes 34 different uranium-based crystals: U_2C_3, U_3As_4, U_3Bi_4, U_3Sb_4, UAl_2, UAl_3, UAs_2, UB_2, UB_4, UBi, UCo_2, UFe_2, UGa_3, UGe_2, UGe_3, UIn_3, UIr_2, UIr_3, UIr, UMn_2, UNi_2, UPb_3, UPd_3, UPt_2, UPt_5, UPt, URh_3, US, USb, USe, USi_3, USn_3, UTe, and UTl_3. These are not present in either of the datasets (I and II) used in model development reported above. The top five most common structure types in this list belong to cubic crystal family with space-group numbers 221, 220, 225, 227, and 191. There are 8 compounds that exhibit AFM, 10 with FM, and the rest have PM ordering at low temperatures. For ordering, the average (based on the ML model built on dataset II) accuracy is 70.1% as predicted for all 34 compounds, shown in Figs. 6(a) and 6(b). While the confusion matrix provides the number of entries with respective true and predicted classes, the bar chart reports the probability of each compound belonging to either PM, FM, or AFM, summing up to 1% or 100%.

External set II has a total of 43 entries of 35 unique neptunium-based compounds: $NpAl_2$, $NpAl_3$, $NpAl_4$, $NpGa_2$, $NpGa_3$, $NpIn_3$, $NpIr_2$, Np_2N_3, $NpNi_2$, Np_2O_5, Np_2Se_5, Np_3S_5, Np_3Se_5 NpAs, $NpAs_2$, NpB_2, NpC, NpCo, $NpFe_2$, $NpGe_3$, $NpIn_3$, $NpMn_2$, NpN, NpN_2, $NpNi_2$, NpO_2, $NpOs_2$, NpP, $NpPd_3$, NpS, NpSb, $NpSb_2$, $NpSi_2$, $NpSi_3$, and $NpSn_3$. All 43 entries are considered for predictions of magnetic ordering using the ML model built on dataset II. As shown in Fig. 6(c), there are total of 18 AFM, 23 FM, and 2 PM compounds present in this set. Out of all AFM compounds, 14 are predicted with the highest probability belonging to

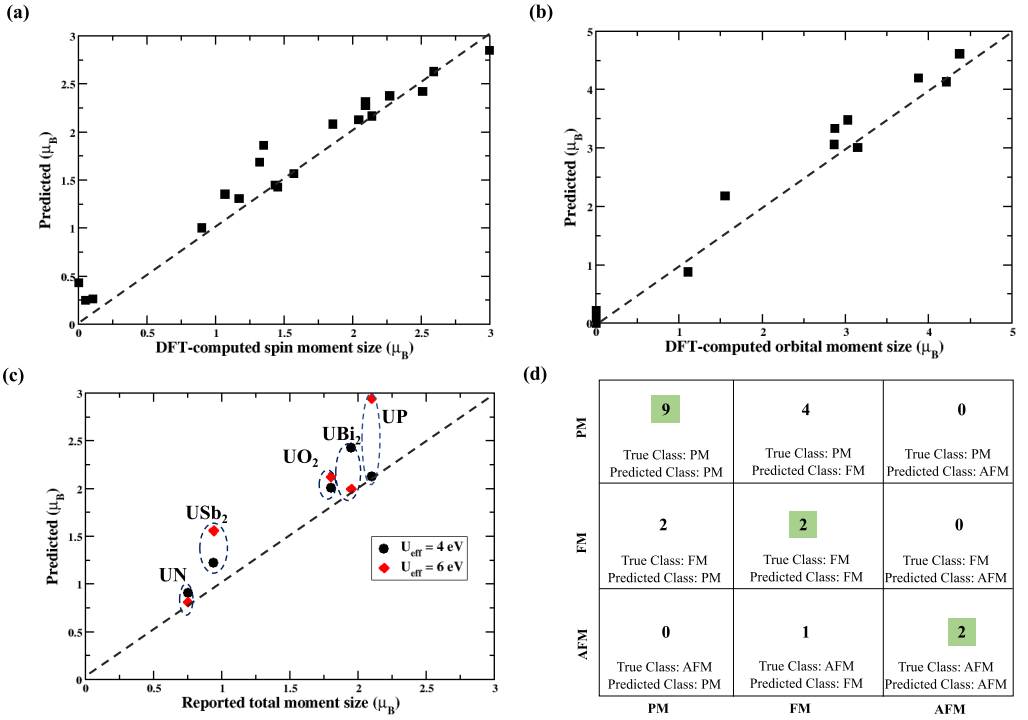

FIG. 5. ML model predictions of (a) spin and (b) orbital moment size for the *internal* validation set from dataset I. A comparison between experimentally reported and predicted total moment size is presented in (c) for compounds in the validation set for which the moment sizes are reported in the literature. The average RMSEs for the prediction of total moment size for these compounds are $0.32\mu_B$ and $0.35\mu_B$ for $U_{eff} =$ 4 and 6 eV, respectively. Magnetic ordering of compounds present in the internal validation set was predicted utilizing a classification model constructed on dataset II. The confusion matrix shown in (d) aggregates the true and predicted ordering classes for each entry with 70.2% average accuracy.

the true class, whereas for FM and PM, there are total of 16 compounds with correct classification of ordering prediction with average accuracy of 67.5%. The most common structure type among these compounds is rocksalt cubic, followed by Laves phase cubic and auricupride. These three structure types are also common among compounds in datasets I and II. Hence, this suggests that the developed ML models may be capable of predicting the end points with similar accuracy as reported earlier in the section.

External set III containing ternary compounds has 136 different entries, out of which 57 exhibit AFM ordering, 39 show FM ordering, and the rest are paramagnetic at low temperatures. These compounds commonly belong to families of orthorhombic, tetragonal, hexagonal, and cubic crystal systems, with the five most common space groups being 62, 139, 123, 127, and 189. For the determination of ordering, the average (based on the ML model built on dataset II) accuracy is 68.9% as predicted for all 136 compounds, shown in Figs. 6(e) and 6(f).

The list of compounds present in the *external* set III and dataset II is given in the Supplemental Material [79]. Overall, the ML-based models built on datasets I and II are capable of delivering reasonable predictions of moment size and ordering for actinide-based binary and ternary compounds.

The following observation is in order: We note that a regression-based ML framework (such as models based on the RFR algorithm) is equally suited to predict magnetic ordering as the classification-based one discussed above. From Figs. 4(a)–4(e), it is evident that the experimental descriptors are capable of dividing dataset II according to each class of ordering and moment size. The difference in the number of compounds exhibiting a specific type of ordering is varied according to median of the descriptor values, meaning larger difference for a particular descriptor should lead to a greater variance when used in decision-tree-type algorithms (such as RFR). This was one of the primary reasons for evaluating such framework for ordering predictions, as detailed in the Supplemental Material [79]. Instead of partitioning the compounds into three classes and predicting those, dataset II can utilize labels 1, 2, and 3 to represent PM, FM, and AFM ordering. In that case, a score corresponding to each entry can be predicted with a certain RMSE. Later, a clustering algorithm can be employed to partition these compounds into PM, FM, or AFM classes. The average RMSE for predicting the ordering with this scheme is 0.12, which is comparable to the accuracy achieved using the RFC algorithm. The OFM representation plays a key role in significantly improving the model performance (RMSE reduced by ∼30%) in predicting magnetic ordering, in the same fashion as already discussed above. Our regression-algorithm-based ML framework can predict numerical scores for partitioning compounds into AFM, FM, and PM ordering classes with an average RMSE of 0.15 for structures in the *internal* validation set of dataset II. The average RMSEs are 0.23 (based on the ML model built on dataset II), 0.14, and 0.24, respectively, as predicted for all compounds listed in *external* validation sets I, II, and III.

These prediction accuracies are comparable with those obtained using the classification approach. Moreover, since

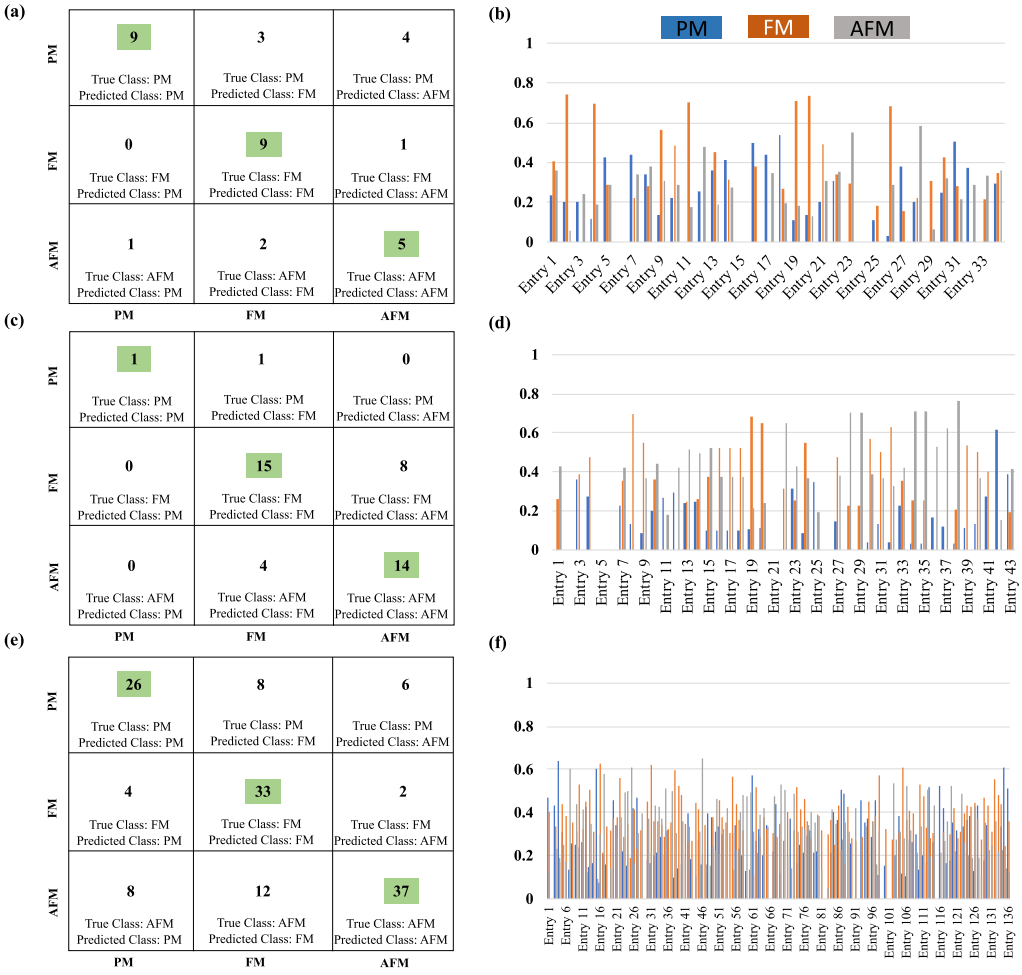

FIG. 6. ML model predictions of magnetic ordering for three external validation sets including uranium-based binary (row 1), neptunium-based binary (row 2), and uranium-based ternary compounds (row 3) represented by confusion matrices (a), (c), (e) and charts (b), (d), (f) showing probabilities for each compound to belong to a specific ordering class. The average prediction accuracies of these models are 70.1%, 67.5%, and 68.9%, respectively.

classification algorithms treat separate classes as discrete rather than continuous entities, they cannot provide further information on possible phase transitions occurring at low temperatures. Instead, regression-algorithm-based predictions can deliver noninteger scores (e.g., an ordering of 1.5), suggesting that the compound of interest may be near the boundary between the PM and FM phases. UTe_2 compound, present in the *internal* validation set of dataset II, may serve as an example. The classification model assigns it to the PM class. However, the regression algorithm gives it an ordering score of 1.46, which falls between PM and FM, indicating of the existence of FM fluctuations at low temperatures. Recently, this compound has been indeed proposed to be at the verge of a FM phase and have a conventional spin-triplet superconducting pairing [83,84]. In addition, as inferred from the classification model, a representative heavy-fermion magnet UCu_5 with a Neél temperature of ∼12 K [85] belongs to the AFM class, while the regression approach gives it a score of 2.63, which may be indicative of possible phase transitions between multiple ordering phases. Given that the temperature dependence of magnetic properties in heavy-fermion compounds is a known fact, additional physical significance can be attributed to the fractional scores obtained from such ML models.

IV. CONCLUSIONS

In conclusion, we have compiled two datasets containing both computational and experimental reports on magnetic properties of uranium-based binary compounds. Through various data analytics techniques, we have identified several descriptors that are critical for understanding magnetic properties of such systems, even before building any predictive models. These insights were then used in developing families of machine learning models to predict the magnetic moment size and ordering. We have also extended this approach to other actinides and assessed the performance of the models. Currently, the models trained on dataset I can only predict moment size for AFM ordered structures. Predicting magnetic spin texture based on the strength of nearest- and next-nearest-neighbor exchange interactions requires additional DFT computations for other magnetic configurations, which is beyond the scope of this work but nonetheless could be

accomplished. Overall, this general prescription, employing both computational and experimental results to construct machine learning models describing magnetism in actinide-based materials, helps us develop better understanding of structure-property relationships that may exist in such complicated structures.

ACKNOWLEDGMENTS

A.G. acknowledges the hospitality of Los Alamos National Laboratory, where this project was initialized. She is also thankful to Dr. L. Louis, D. P. Trujillo, Dr. G. Pilania, and Dr. G. P. F. Wood for their helpful contributions to code development and discussions on implementation of various machine learning techniques. This work was supported by the U. S. DOE NNSA under Contract No. 89233218CNA000001 through the Rapid Response Program of Institute for Materials Science at LANL (A.G.), by the DOE BES "Quantum Fluctuations in Narrow-Band System" Project (F.R), and the NNSA Advanced Simulation and Computing Program (J.-X.Z.). It was supported in part through the Center for Integrated Nanotechnologies, a U. S. DOE Office of Basic Energy Sciences user facility in partnership with the LANL Institutional Computing Program for computational resources.

[1] K. Rajan, Annu. Rev. Mater. Res. **45**, 153 (2015).
[2] T. Mueller, A. G. Kusne, and R. Ramprasad, Rev. Comput. Chem. **29**, 186 (2016).
[3] K. T. Butler, D. W. Davies, H. Cartwright, O. Isayev, and A. Walsh, Nature (London) **559**, 547 (2018).
[4] J. Graser, S. K. Kauwe, and T. D. Sparks, Chem. Mater. **30**, 3601 (2018).
[5] M. Rupp, Int. J. Quantum Chem. **115**, 1058 (2015).
[6] A. Jain, S. P. Ong, G. Hautier, W. Chen, W. D. Richards, S. Dacek, S. Cholia, D. Gunter, D. Skinner, G. Ceder *et al.*, APL Mater. **1**, 011002 (2013).
[7] S. P. Ong, S. Cholia, A. Jain, M. Brafman, D. Gunter, G. Ceder, and K. A. Persson, Comput. Mater Sci. **97**, 209 (2015).
[8] J. Behler, J. Chem. Phys. **134**, 074106 (2011).
[9] Z. D. Pozun, K. Hansen, D. Sheppard, M. Rupp, K.-R. Müller, and G. Henkelman, J. Chem. Phys. **136**, 174101 (2012).
[10] B. Meredig, A. Agrawal, S. Kirklin, J. E. Saal, J. W. Doak, A. Thompson, K. Zhang, A. Choudhary, and C. Wolverton, Phys. Rev. B **89**, 094104 (2014).
[11] T. D. Huan, A. Mannodi-Kanakkithodi, and R. Ramprasad, Phys. Rev. B **92**, 014106 (2015).
[12] G. Pilania, P. Balachandran, J. E. Gubernatis, and T. Lookman, Acta Crystallogr., Sect. B **71**, 507 (2015).
[13] A. Seko, H. Hayashi, K. Nakayama, A. Takahashi, and I. Tanaka, Phys. Rev. B **95**, 144110 (2017).
[14] V. Stanev, C. Oses, A. G. Kusne, E. Rodriguez, J. Paglione, S. Curtarolo, and I. Takeuchi, Npj Comput. Mater. **4**, 29 (2018).
[15] A. O. Oliynyk, E. Antono, T. D. Sparks, L. Ghadbeigi, M. W. Gaultois, B. Meredig, and A. Mar, Chem. Mater. **28**, 7324 (2016).
[16] A. O. Oliynyk and A. Mar, Acc. Chem. Res. **51**, 59 (2017).
[17] F. Faber, A. Lindmaa, O. A. von Lilienfeld, and R. Armiento, Int. J. Quantum. Chem. **115**, 1094 (2015).
[18] G. Pilania, A. Mannodi-Kanakkithodi, B. Uberuaga, R. Ramprasad, J. Gubernatis, and T. Lookman, Sci. Rep. **6**, 19375 (2016).
[19] A. Ghosh, L. Louis, K. K. Arora, B. C. Hancock, J. F. Krzyzaniak, P. Meenan, S. Nakhmanson, and G. P. Wood, Cryst. Eng. Commun. **21**, 1215 (2019).
[20] Y.-C. Lo, S. E. Rensi, W. Torng, and R. B. Altman, Drug Discovery Today **23**, 1538 (2018).
[21] J. S. Smith, A. E. Roitberg, and O. Isayev (unpublished).
[22] D. Fourches, E. Muratov, and A. Tropsha, Nat. Chem. Biol. **11**, 535 (2015).
[23] D. Fourches, E. Muratov, and A. Tropsha, J. Chem. Inf. Model. **56**, 1243 (2016).
[24] M. Rupp, A. Tkatchenko, K.-R. Müller, and O. A. von Lilienfeld, Phys. Rev. Lett. **108**, 058301 (2012).
[25] J. T. Lopuszanski, A. Pekalski, and J. Przystawa, *Magnetism in Metals and Metallic Compounds* (Springer, Berlin, 1976).
[26] K. Gurtovoi and R. Levitin, Phys. Usp. **30**, 827 (1987).
[27] P. Santini, R. Lemanski, and P. Erdős, Adv. Phys. **48**, 537 (1999).
[28] R. A. Layfield and M. Murugesu, *Lanthanides and Actinides in Molecular Magnetism* (Wiley, Weinheim, 2015).
[29] M. Jaime, A. Saúl, M. Salamon, V. Zapf, N. Harrison, T. Durakiewicz, J. Lashley, D. Andersson, C. Stanek, J. Smith *et al.*, Nat. Commun. **8**, 99 (2017).
[30] P. Wölfle, J. Magn. Magn. Mater. **76**, 492 (1988).
[31] M. Sigrist and K. Ueda, Rev. Mod. Phys. **63**, 239 (1991).
[32] V. P. Mineev, K. Samokhin, and L. Landau, *Introduction to Unconventional Superconductivity* (CRC Press, Boca Raton, FL, 1999).
[33] C. Pfleiderer, Rev. Mod. Phys. **81**, 1551 (2009).
[34] M. R. Norman, Science **332**, 196 (2011).
[35] B. White, J. Thompson, and M. Maple, Phys. C (Amsterdam) **514**, 246 (2015).
[36] Y. Cao, V. Fatemi, S. Fang, K. Watanabe, T. Taniguchi, E. Kaxiras, and P. Jarillo-Herrero, Nature (London) **556**, 43 (2018).
[37] N. Mott, Rev. Mod. Phys. **40**, 677 (1968).
[38] B. Johansson, Phys. Rev. B **11**, 2740 (1975).
[39] P. Gegenwart, Q. Si, and F. Steglich, Nat. Phys. **4**, 186 (2008).
[40] K. T. Moore and G. van der Laan, Rev. Mod. Phys. **81**, 235 (2009).
[41] O. Stockert and F. Steglich, Annu. Rev. Condens. Matter Phys. **2**, 79 (2011).
[42] P. Erdos, *The Physics of Actinide Compounds* (Springer, Berlin, 2012).
[43] G. T. Seaborg, J. J. Katz, and L. R. Morss, *The Chemistry of the Actinide Elements*, Vol. 2 (Springer, Cham, 2012).
[44] G. L. Verschuur, *Hidden Attraction: The History and Mystery of Magnetism* (Oxford University Press, Oxford, 1996).
[45] J. O. Stenflo, Nature (London) **430**, 304 (2004).
[46] T. Park, F. Ronning, H. Yuan, M. Salamon, R. Movshovich, J. Sarrao, and J. Thompson, Nature (London) **440**, 65 (2006).
[47] J. A. Mydosh and P. M. Oppeneer, Rev. Mod. Phys. **83**, 1301 (2011).

[48] J. A. Mydosh and P. M. Oppeneer, Philos. Mag. **94**, 3642 (2014).

[49] H.-H. Kung, R. Baumbach, E. Bauer, V. Thorsmølle, W.-L. Zhang, K. Haule, J. Mydosh, and G. Blumberg, Science **347**, 1339 (2015).

[50] M. S. Chanowitz, M. Furman, and I. Hinchliffe, Nucl. Phys. B **153**, 402 (1979).

[51] S. G. Stewart, Rev. Mod. Phys. **56**, 755 (1984).

[52] C. Varma, Phys. Rev. Lett. **55**, 2723 (1985).

[53] B. Batlogg, D. Bishop, E. Bucher, B. Golding, Jr., A. Ramirez, Z. Fisk, and J. Smith, *Anomalous Rare Earths and Actinides* (Elsevier, Amsterdam, 1987), pp. 441–446.

[54] N. Grewe and F. Steglich, Handbook Phys. Chem. Rare Earths **14**, 343 (1991).

[55] A. C. Hewson, *The Kondo Problem to Heavy Fermions*, Vol. 2 (Cambridge University Press, Cambridge, 1997).

[56] G. Stewart, Rev. Mod. Phys. **73**, 797 (2001).

[57] G. R. Stewart, Rev. Mod. Phys. **78**, 743 (2006).

[58] G. Bihlmayer, G. Stollhoff, A. Lichtenstein, M. Katsnelson, F. Assaad, M. Troyer, P. Coleman, B. Jones, P. Horsch, S. Sachdev *et al.*, *Handbook of Magnetism and Advanced Magnetic Materials* (Wiley, Hoboken, NJ, 2007).

[59] Q. Si and F. Steglich, Science **329**, 1161 (2010).

[60] L. C. Gupta, *Theoretical and Experimental Aspects of Valence Fluctuations and Heavy Fermions* (Springer, New York, 2012).

[61] G. Hautier, C. C. Fischer, A. Jain, T. Mueller, and G. Ceder, Chem. Mater. **22**, 3762 (2010).

[62] M. K. Horton, J. H. Montoya, M. Liu, and K. A. Persson, Npj Comput. Mater. **5**, 64 (2019).

[63] C. M. Bishop, *Pattern Recognition and Machine Learning* (Springer, New York, Springer, 2006).

[64] I. Goodfellow, Y. Bengio, and A. Courville, *Deep Learning* (MIT Press, Cambridge, MA, 2016).

[65] G. Kresse and J. Hafner, Phys. Rev. B **47**, 558 (1993).

[66] G. Kresse and J. Furthmüller, Phys. Rev. B **54**, 11169 (1996).

[67] S. Dudarev, G. Botton, S. Y. Savrasov, Z. Szotek, W. Temmerman, and A. Sutton, Phys. Status Solidi A **166**, 429 (1998).

[68] H. J. Monkhorst and J. D. Pack, Phys. Rev. B **13**, 5188 (1976).

[69] R. Troć, J. Leciejewicz, and R. Ciszewski, Phys. Status Solidi B **15**, 515 (1966).

[70] S. Lebègue, P. M. Oppeneer, and O. Eriksson, Phys. Rev. B **73**, 045119 (2006).

[71] F. Zhou and V. Ozoliņš, Phys. Rev. B **83**, 085106 (2011).

[72] X.-D. Wen, R. L. Martin, G. E. Scuseria, S. P. Rudin, E. R. Batista, and A. K. Burrell, J. Phys.: Condens. Matter **25**, 025501 (2012).

[73] A. Belsky, M. Hellenbrandt, V. L. Karen, and P. Luksch, Acta Crystallogr. Sect. B **58**, 364 (2002).

[74] R. Batra, G. Pilania, B. P. Uberuaga, and R. Ramprasad, ACS Appl. Mater. Int. **11**, 24906 (2019).

[75] T. L. Pham, H. Kino, K. Terakura, T. Miyake, K. Tsuda, I. Takigawa, and H. C. Dam, Sci. Technol. Adv. Mater. **18**, 756 (2017).

[76] T.-L. Pham, N.-D. Nguyen, V.-D. Nguyen, H. Kino, T. Miyake, and H.-C. Dam, J. Chem. Phys. **148**, 204106 (2018).

[77] L. Ward, A. Dunn, A. Faghaninia, N. E. Zimmermann, S. Bajaj, Q. Wang, J. Montoya, J. Chen, K. Bystrom, M. Dylla *et al.*, Comput. Mater. Sci. **152**, 60 (2018).

[78] R Core Team, *R: A Language and Environment for Statistical Computing* (R Foundation for Statistical Computing, Vienna, Austria, 2018).

[79] See Supplemental Material at http://link.aps.org/supplemental/10.1103/PhysRevMaterials.4.064414 for structural parameters of 12 compounds utilized to construct Dataset I. Information on correlation matrices for primary and compound features, decision trees, optimized hyperparameters for generating ML models, comparative learning curves, compounds present in validation sets are listed here. Hill limit comparisons along with predictions on ordering obtained using regression-based predictive models can also be found in this document.

[80] F. Pedregosa, G. Varoquaux, A. Gramfort, V. Michel, B. Thirion, O. Grisel, M. Blondel, P. Prettenhofer, R. Weiss, V. Dubourg, J. Vanderplas, A. Passos, D. Cournapeau, M. Brucher, M. Perrot, and E. Duchesnay, J. Mach. Learn. Res. **12**, 2825 (2011).

[81] H. H. Hill, *Early Actinides: The Periodic System's f Electron Transition Metal Series*, in Plutonium 1970 and Other Actinides (AIME, New York, 1970).

[82] V. Sechovsky and L. Havela, Handbook Magn. Mater. **11**, 1 (1998).

[83] S. Sundar, S. Gheidi, K. Akintola, A. M. Cote, S. R. Dunsiger, S. Ran, N. P. Butch, S. R. Saha, J. Paglione, and J. E. Sonier, Phys. Rev. B **100**, 140502(R) (2019).

[84] S. Ran, C. Eckberg, Q.-P. Ding, Y. Furukawa, T. Metz, S. R. Saha, I.-L. Liu, and M. Zic, Science **365**, 684 (2019).

[85] M. R. Norman, B. I. Min, T. Oguchi, and A. J. Freeman, Phys. Rev. B **38**, 6818 (1988).